

Article

Numerical Modeling of Elastic Wave Propagation in Porous Soils with Vertically Inhomogeneous Fluid Contents Due to Infiltration

Sergey I. Fomenko ^{1,*} , Raghavendra B. Jana ²  and Mikhail V. Golub ¹ 

¹ Institute for Mathematics, Mechanics and Informatics, Kuban State University, 350040 Krasnodar, Russia; m_golub@inbox.ru

² Center for AgroTechnologies, Skolkovo Institute of Science and Technology, 121205 Moscow, Russia; r.jana@skoltech.ru

* Correspondence: sfom@yandex.ru

Abstract: The structure of soils is often heterogeneous with layered strata having distinct permeabilities. An advanced mathematical and numerical coupled model of elastic wave propagation in poroelastic multi-layered soils subjected to subsoil water infiltration is proposed in this study. The coupled model was based on the introduction of an inhomogeneous functionally graded fluid-saturation of the considered soil depending on the infiltration time, which was evaluated employing Richards' equation. The time-harmonic solution was formulated in terms of the Fourier transform of Green's matrix and the surface load that excites the vibration. The convergence and efficiency of the proposed approach are demonstrated. An example of dispersion curves for partially saturated porous strata made of loam, sand, and rock at different infiltration times is provided, and it is shown that the characteristics of the surface acoustic waves change with time, which can be further used for inverse problems' solution.

Keywords: guided waves; poroelastic layered media; Biot's equations; infiltration; Richards' equations

MSC: 74B05; 74F10; 74E05; 74H10; 74J15



Citation: Fomenko, S.I.; Jana, R.B.; Golub, M.V. Numerical Modeling of Elastic Wave Propagation in Porous Soils with Vertically Inhomogeneous Fluid Contents Due to Infiltration. *Mathematics* **2023**, *11*, 4131. <https://doi.org/10.3390/math11194131>

Academic Editor: Nikolaos L. Tsitsas

Received: 30 August 2023
Revised: 23 September 2023
Accepted: 25 September 2023
Published: 29 September 2023



Copyright: © 2023 by the authors. Licensee MDPI, Basel, Switzerland. This article is an open access article distributed under the terms and conditions of the Creative Commons Attribution (CC BY) license (<https://creativecommons.org/licenses/by/4.0/>).

1. Introduction

Controlling fluid transport within subsurface porous media is crucial to many environmental and industrial studies from agriculture to geophysics. Therefore, efficient mathematical and computer models accurately simulating their behavior are required. Complex engineering problems currently can be solved using robust numerical methods such as the finite element method, as well as the spectral element method, the boundary element method, the finite volume method, and meshless methods. Various coupling procedures (hybrid and coupled numerical methods) have been proposed incorporating different numerical methods in order to take advantage of their respective benefits [1–3].

The structure of real porous media is often heterogeneous with layered strata with distinct permeabilities causing uneven flow partitioning across the strata. Developing more-advanced interpretation tools is hindered by the lack of open-source and semi-analytical numerical techniques for simulating partially saturated porous media [4]. Thus, the aim of this study was to develop an advanced mathematical and numerical coupled model of elastic wave propagation in poroelastic multi-layered soil subjected to subsoil water infiltration.

Sufficient soil water content, which is a key requirement for good agricultural yields, depends on numerous factors. First of all, there are the temperature and humidity of the environment leading either to the evaporation of moisture from the soil or, vice versa, contributing to the saturation of the soil with water [5,6]. The soil hydrology is also a significant factor, which depends on the soil texture and structure [7,8].

The water infiltration process in variably saturated soil pores as described by Richards' equation demonstrates the complex nonlinear distributions of porous water content with soil depth and is dependent on the material parameters of the composite (solid and complex fluid as a combination of air and water), initial water saturation, and time of infiltration [9]. Soil water dynamics are simulated using various numerical methods from the finite element method [10–12] and Bayesian inverse modeling using Markov chain Monte Carlo [13,14] to machine learning-based methods. For instance, Yang and Mei [15], Jana et al. [16] employed physics-informed neural-network-based numerical approaches for studying soil water vertical infiltration. Other approaches include using pore-scale simulations with X-ray tomography [17] and continuum approaches using volumetric averaging [18]. A comparison of some different traditionally used models for soil water infiltration such as the Philip model, Kostiakov model, Mezencev model, USDA-NRCS model, and Horton model can be found in [19]. The latest techniques in field estimation of soil water infiltration include the use of electrical resistivity tomography (ERT) and ground-penetrating radar (GPR) [20].

The theoretical study of elastic wave propagation in fluid-saturated porous media is based on the boundary-value problem for Biot's equation [21–23]. To solve the wave problems for poroelastic structures with complex irregular boundaries and obstacles, the following numerical methods have been developed: the boundary element method (BEM) [24,25], the finite element method [26–28], and its modifications as the spectral element method [29,30], extended finite elements [31,32], or particle finite elements [33,34], as well as meshless methods [35,36]. Waves in poroelastic structures with traditional regular boundaries are usually investigated by analytical and semi-analytical methods. The description of such methods to analyze waves excited in poroelastic isotropic structures with plane-parallel boundaries such as half-spaces or layered spaces and the analysis of guided waves in the layered media can be found in [37–42]. The matrix iteration methods for modeling waves in multilayered porous media were developed in [43,44]. The wave propagation in functionally graded poroelastic fluid-saturated media have also been actively studying recently [45–48] by semi-analytical approaches. Dudarev et al. [45] also developed and studied the method for the reconstruction of Biot's modulus as spatial function using elastic waves measured on the surface of a poroelastic functionally graded cylinder. The analytical solution of a multi-layered structure satisfies the conditions at infinity and allows studying guided waves, as well as can be used as a basis for boundary integral equation methods and the BEM for layered structures with irregularities [49–51].

Chen et al. [52] investigated the correlation between soil moisture changes and deformations at slope surfaces by means of elastic wave propagation in soils. Their analysis of longitudinal and shear wave velocities in homogeneous media showed that the elastic wave velocity continuously decreases in response to moisture content and deformation. Chen et al. [53] estimated the elastic wave velocity of an unsaturated soil slope, and they showed that the effects of rainfall duration/initial water content, density, slope angle, and surface layer thickness on the decrease rate of the normalized wave velocity with the volumetric water content and the tilt angle are relatively small in homogeneous media. Solazzi et al. [54] assumed a one-dimensional unconsolidated porous half-space under steady-state saturation conditions and considered the influence of the capillary suction effects on the longitudinal and shear wave dispersion characteristics for different water table depths and overlying soil textures. Recently, Deng et al. [55] presented Biot's model with two fluid phases and also studied body waves in vertically inhomogeneous saturated porous media resulting from porous water infiltration. To the authors' knowledge, the surface wave propagation problem was not considered taking into account the infiltration effect.

Therefore, we propose here a semi-analytical two-stage numerical method for modeling wave propagation in multi-layered porous media with properties varying across the strata and taking into account the infiltration effect. In the first stage, the depth and time-dependent saturation were evaluated employing Richards' equation. Then, an in-

homogeneous functionally graded fluid saturation was transferred into Biot’s equations, which were solved via the semi-analytical boundary integral equation method at various infiltration times. The algorithm for Green’s matrix of multi-layered porous solids [41] was improved in this investigation in terms of numerically stable matrix iterations for the considered vertically stratified (functionally graded) medium [56]. The convergence and efficiency of the method are demonstrated. Examples of dispersion curves for partially saturated porous strata made of loam, sand, and bedrock at different infiltration times are provided, and it is shown that the characteristics of surface acoustic waves change with time, which can be further used for inverse problems’ solution. The model also assists in the investigation of the influence of infiltration time on wave propagation in porous media.

2. Mathematical Models

2.1. Elastic Waves in a Layered Poroelastic Soil

The wave propagation generated by the surface load of an inhomogeneous soil modeled by a three-layered half-space was considered (Figure 1). Further, we used the designation for a layer as $\mathbb{L}(\mathcal{M}, z_1, z_2)$, where \mathcal{M} is the set of material properties and z_1 and z_2 are the z -coordinates in the Cartesian coordinate system (x, y, z) (or (x_1, x_2, x_3) as the same) of the planes bounding the layer. The layered half-space $\mathbb{HS} = \mathbb{L}_{loam} \cup \mathbb{L}_{sand} \cup \mathbb{L}_{rock}$ consists of two poroelastic layers $\mathbb{L}_{loam} = \mathbb{L}(\mathcal{M}_{loam}, 0, z_1)$, $\mathbb{L}_{sand} = \mathbb{L}(\mathcal{M}_{sand}, z_1, z_2)$ with thicknesses a_1 and a_2 , $z_1 = -a_1$ and $z_2 = -a_1 - a_2$, consequently, and the bottom pure elastic homogeneous half-space $\mathbb{L}_{rock} = \mathbb{L}(\mathcal{M}_{rock}, z_2, -\infty)$. The first poroelastic layer \mathbb{L}_{loam} models the loam with vertically inhomogeneous fluid contents due to water infiltration and air saturation of the vacated pore space. The infiltration is a dynamical process; however, its speed is much less than the speed of the elastic waves; therefore, the properties of the first layer are considered to be fixed during the measurements of elastic waves.

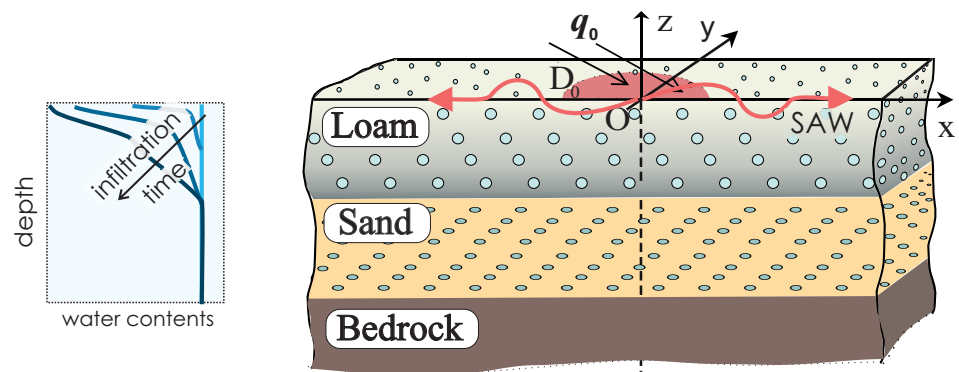


Figure 1. Multilayered poroelastic soil with functionally graded saturation.

The steady-state harmonic waves with frequency ω were considered further ($u(t) = u(\omega) \exp(-i\omega t)$). The displacements in a poroelastic medium according to Biot [21] are expressed in terms of two complex-valued displacement vectors u_s and u_f in the solid skeleton and porous fluid, respectively. The displacements are governed by Biot’s equations in the frequency domain:

$$\begin{aligned} \nabla[(\lambda + \mu)\nabla \cdot u_s + Q \nabla \cdot u_f] + \mu \nabla^2 u_s + \hat{\rho}_{11} \omega^2 u_s + \hat{\rho}_{12} \omega^2 u_f &= 0, \\ \nabla[Q \nabla \cdot u_s + R \nabla \cdot u_f] + \hat{\rho}_{12} \omega^2 u_s + \hat{\rho}_{22} \omega^2 u_f &= 0. \end{aligned} \tag{1}$$

The complex amplitudes of the traction vector τ_n at a surface element with normal n are given as

$$\begin{aligned} \tau_n &= \tau_{s;n} - \phi p_f n \\ \tau_{s;n} &= [\lambda \nabla \cdot \mathbf{u}_s + Q \nabla \cdot \mathbf{u}_f] n + 2\mu \nabla \mathbf{u}_s \cdot n + \mu (n \times \nabla \times \mathbf{u}_s) \\ p_f &= -\frac{1}{\phi} [Q \nabla \cdot \mathbf{u}_s + R \nabla \cdot \mathbf{u}_f]. \end{aligned} \tag{2}$$

Here, $\tau_{s;n}$ is the traction (stress) of the solid skeleton, p_f is the pore fluid pressure, ∇ is the nabla operator, “ \cdot ” and “ \times ” are operators of the dot and cross products, respectively, and λ, μ, Q, R are Biot’s poroelastic constants. The coefficients $\hat{\rho}_{mn} = \rho_{mn} - i(-1)^{m+n}b/\omega$ are expressed in terms of the effective mass densities ρ_{11}, ρ_{22} , and $\rho_{12} = \rho_{21}$ and the dissipation factor b . The relative displacements of the fluid as $w = \phi(\mathbf{u}_s - \mathbf{u}_f)$ needs further for analysis.

In practice, the parameters of poroelastic materials (\mathcal{M}_{loam} and \mathcal{M}_{sand}) are presented by the specific porosity ϕ , shear modulus μ , the bulk modulus of dried porous material K_d , the bulk modulus K_s, K_f , and the mass densities ρ_s, ρ_f of the solid skeleton and porous fluid, consequently, as well as the tortuosity parameter α_s , the intrinsic permeability κ_s , and the dynamic viscosity of the fluid η_f . The parameters of Equations (1) and (2) are expressed as

$$\begin{aligned} Q &= \phi(1 - \phi - K_d/K_s)\Lambda, \quad R = \phi^2\Lambda, \\ \lambda &= K_d + Q^2/R - 2/3\mu, \quad \Lambda = K_s/(1 - \phi - K_d/K_s + \phi K_s/K_f); \\ \rho_{12} &= \phi\rho_f(1 - \alpha_s), \quad \rho_{11} = \rho_s(1 - \phi) + \rho_{12}, \\ \rho_{22} &= \rho_f\phi - \rho_{12}, \quad b = \eta_f\phi^2/\kappa_s. \end{aligned} \tag{3}$$

The pore fluid in the top layer \mathbb{L}_{loam} is vertically functionally graded due to infiltration, which leads to homogeneous water saturation $\zeta(z)$. Let ρ_w, K_w, η_w and ρ_a, K_a, η_a be the mass densities, the bulk modulus, and the viscosities of water and air, respectively. One of the conventional approaches is to consider a homogenized fluid. Applying the mixing theory to water and air, the effective bulk modulus K_f , mass density ρ_f , and viscosity η_f are taken as [23,57]

$$\frac{1}{K_f} = \frac{\zeta}{K_w} + \frac{1 - \zeta}{K_a}, \quad \rho_f = \rho_w\zeta + \rho_a(1 - \zeta), \quad \eta_f = \eta_w^\zeta \eta_a^{1-\zeta}, \tag{4}$$

The displacements \mathbf{u}_s and tensions τ_n in the pure elastic bottom half-space obey the Lamé equations and Hooke’s law as follows:

$$\begin{aligned} \nabla[(\lambda + \mu)\nabla \cdot \mathbf{u}_s] + \mu \nabla^2 \mathbf{u}_s + \rho_s \omega^2 \mathbf{u}_s &= 0, \\ \tau_n &= \lambda \nabla \cdot \mathbf{u}_s n + 2\mu \nabla \mathbf{u}_s \cdot n + \mu (n \times \nabla \times \mathbf{u}_s) \end{aligned} \tag{5}$$

The excitation of elastic waves is caused by the surface load given by axisymmetric traction $\mathbf{q}(x, y) = q(r), r^2 = x^2 + y^2$, at some finite circular region Ω as

$$\tau_3 = q, \quad p_f = q_3, \text{ at } z = 0, (x, y) \in \Omega. \tag{6}$$

The displacement \mathbf{u}_s and tension τ_3 vectors are continuous at the interfaces between layers. The continuity of the normal component of the relative phase displacements w_3 and porous fluid pressure p_f are additionally imposed at the porous–porous interface as

$$[\mathbf{u}_s] = 0, [\tau_3] = 0, [w_3] = 0, [p_f] = 0 \text{ at } z = z_1. \tag{7}$$

At the interface between the porous layer and elastic half-space, the relative phase displacements w_3 is eliminated:

$$[u_s] = 0, [\tau_3] = 0, [w_3] = 0 \text{ at } z = z_2. \tag{8}$$

Describing correctly waves at infinity, such radiation conditions as the limiting absorption principle [58] were used.

2.2. Mathematical Model of Water Infiltration into Porous Soil

The water flow in porous media is governed by Richards' equation:

$$\frac{\partial \theta}{\partial t} = \frac{\partial}{\partial x_i} \left[\mathcal{K} \left(\mathcal{K}_{ij}^A \frac{\partial h}{\partial x_j} + \mathcal{K}_{iz}^A \right) \right] - \mathcal{S} \tag{9}$$

written in terms of the volumetric water content θ , the pressure head h , and the unsaturated hydraulic conductivity:

$$\mathcal{K}(h, x_1, x_2, x_3) = \mathcal{K}_s(x_1, x_2, x_3) \mathcal{K}_r(h, x_1, x_2, x_3) \tag{10}$$

which is the function of the saturated hydraulic conductivity \mathcal{K}_s and the relative hydraulic conductivity \mathcal{K}_r . Here, Cartesian coordinates x_i ($i = 1, 2, 3$) were considered; as before, t is the time of water infiltration, \mathcal{K}^A is an anisotropy tensor, and \mathcal{S} is a sink term.

The water content $\theta(h)$ and hydraulic conductivity $\mathcal{K}(h)$ are unsaturated soil hydraulic properties that are highly non-linear functions of the pressure head h . Different analytical models exist to compute these quantities. However, the formulation of Van Genuchten [9] offers a reasonable balance between accuracy and model complexity. Hence, this formulation is used in this study. According to the van Genuchten model, water content and hydraulic conductivity are expressed in terms of the residual water content θ_r , the saturation water content θ_s , the inverse of the air-entry pressure α_h , the pore-size distribution index n , and the effective water content:

$$S_e = \frac{\theta - \theta_r}{\theta_s - \theta_r} \tag{11}$$

The pore connectivity parameter l is as follows:

$$\theta(h) = \begin{cases} \theta_r + \frac{\theta_s - \theta_r}{[1 + |\alpha_h h|^n]^m}, & h < 0 \\ \theta_s, & h \geq 0 \end{cases} \tag{12}$$

$$\mathcal{K}(h) = \mathcal{K}_s S_e^l \left[1 - \left(1 - S_e^{\frac{1}{m}} \right)^m \right]^2 \tag{13}$$

Here,

$$m = 1 - \frac{1}{n}, \quad n > 1.$$

The parameters α and n are considered empirical shape-fitting parameters, and l has been estimated to be equal to 0.5 on average for a wide range of soils.

2.3. Numerical Solution of Richards' Equation

Richards' Equation (9) does not have an analytical solution and is limited to numerical solutions only. In this study, we used the commercially available HYDRUS-3D software package from PC-Progress [59]. HYDRUS uses Galerkin-type linear finite element schemes to numerically solve the water flow equation. The solution to matrix equations derived from the discretization of the governing equations varies based on the problem's magnitude. For banded matrices, Gaussian elimination is employed, while symmetric matrices

utilize the conjugate gradient method, and asymmetric matrices use the ORTHOMIN method. The software can examine the movement of water and solutes in porous media that are unsaturated, partially saturated, or fully saturated. Flow and transport can take place in the vertical or horizontal plane, a three-dimensional area with radial symmetry around the vertical axis, or a fully three-dimensional space. HYDRUS can handle water flow computation for domains having boundaries with a prescribed head and flux, boundaries influenced by atmospheric conditions, free drainage boundary conditions, or more-intricate combinations.

In this study, the soil domain was discretized with three different boundary conditions (BCs). The top surface was assigned an “Atmospheric” BC, while the bottom layer was assigned a “Free Drainage” BC. The side walls of the domain were assigned a “No Flow” BC, resulting in a flow regime that is purely vertical. The first two BCs are described below.

2.3.1. Atmospheric BC

The Atmospheric BC is a system-dependent BC that exists at the interface between the air and the soil that is exposed to atmospheric conditions. The fluid flux at this boundary is driven by external conditions (such as precipitation) and also due to existing soil water content conditions that can be time-dependent. The application of this BC imposes that the numerical solution of (9) is obtained by limiting the absolute water flux in a manner that satisfies the following two conditions:

$$|\mathcal{K}(\mathcal{K}_{ij}^A \frac{\partial h}{\partial x_j} + \mathcal{K}_{iz}^A)n_i| \leq E \quad (14)$$

and

$$h_a \leq h \leq h_s \quad (15)$$

where n_i are components of the outward unit vector normal to the boundary, E is the maximum potential flux rate (infiltration or evaporation), h is the pressure head at the soil surface, h_a is the minimum allowed pressure head determined from the equilibrium between the soil water and the atmospheric water vapor pressure, and h_s is the maximum allowed pressure head, which is generally the condition of complete saturation where the value can be set to zero.

This BC allows for the direction of the water flux at the interface to switch directions depending on the prevailing internal and external conditions. For example, the application of water (by precipitation or irrigation) at the boundary to the soil domain with water content below saturation results in the infiltration (or the downward movement) of the water. On the other hand, the introduction of the effect of temperature allows for the evaporation of water through the boundary (upward movement). In this study, the Atmospheric BC was assigned to ensure the free flow of water through the domain with no upward suction due to the creation of vacuum pockets.

2.3.2. Free Drainage BC

This is a gradient type BC of the form

$$\left(\mathcal{K}_{ij}^A \frac{\partial h}{\partial x_j} + \mathcal{K}_{iz}^A \right) n_i = f(x, y, z, t) \quad (16)$$

Here, HYDRUS implements a unit vertical hydraulic gradient that mimics free water flow through the boundary. Such scenarios are very commonly encountered in field studies where the soil profile is deep and the water table is much below the study domain.

3. Simulation of Wave Propagation in Functionally Graded Poroelastic Media

3.1. Wavefield Representation in a Homogeneous Poroelastic Layer

Let us consider a poroelastic layer $\mathbb{L}(\mathcal{M}_p, z_1, z_2)$, where \mathcal{M}_p is a set of poroelastic parameters. The solution of Biot’s Equation (1) \mathbf{u}_s and \mathbf{u}_f in a homogeneous media can be determined in terms of two scalar potentials φ_1, φ_2 and the curl potential $\boldsymbol{\psi}$ as follows:

$$\mathbf{u}_s = \nabla \varphi_1 + \eta_2 \nabla \varphi_2 + \nabla \times \boldsymbol{\psi}, \tag{17}$$

$$\mathbf{u}_f = \eta_1 \nabla \varphi_1 + \nabla \varphi_2 + \eta_3 \nabla \times \boldsymbol{\psi}.$$

Here, the potentials φ_k ($k = 1, 2$) and $\boldsymbol{\psi} = \{\partial\psi_1/\partial y, -\partial\psi_1/\partial x, \psi_2\}$ obey the Helmholtz equations:

$$\nabla^2 \varphi_k + \varkappa_{pk}^2 \varphi_k = 0, \quad \varkappa_{pk} = \omega/v_{pk}; \quad k = 1, 2 \tag{18}$$

$$\nabla^2 \psi_j + \varkappa_s^2 \psi_j = 0, \quad \varkappa_s = \omega/v_s; \quad j = 1, 2 \tag{19}$$

The fast and slow longitudinal wave velocities v_{pi} , coefficients m_i , and shear velocity v_s in decomposition (17) are determined by the formulas:

$$\begin{aligned} v_{pk}^2 &= [b - (-1)^k \sqrt{b^2 - 4\Delta C \Delta B}] / (2\Delta B), \quad v_s^2 = \mu \hat{\rho}_{22} / \Delta B; \\ \eta_1 &= -(P - v_{p1}^2 \hat{\rho}_{11}) / (Q - v_{p1}^2 \hat{\rho}_{12}), \quad \eta_2 = -(R - v_{p2}^2 \hat{\rho}_{22}) / (Q - v_{p2}^2 \hat{\rho}_{12}), \\ b &= R \hat{\rho}_{11} - 2Q \hat{\rho}_{12} + P \hat{\rho}_{22}, \quad \Delta B = \hat{\rho}_{11} \hat{\rho}_{22} - \hat{\rho}_{12}^2, \\ \Delta C &= PR - Q^2, \quad P = \lambda + 2\mu \end{aligned} \tag{20}$$

and $\eta_3 = -\frac{\hat{\rho}_{12}}{\hat{\rho}_{22}}$ in Equation (17).

Applying the Fourier transform,

$$G(\alpha_1, \alpha_2) = \mathfrak{F}_{x,y}[g] = \iint_{-\infty}^{\infty} g(x, y) e^{i(\alpha_1 x + \alpha_2 y)} dx dy,$$

with respect to coordinates x_1 and x_2 allows us to write the potentials in terms of relations (20) as the general solutions of Equations (18) and (19):

$$\begin{aligned} \Phi_k(\alpha, z) &= \mathfrak{F}_{x,y}[\varphi_k] = t_k^+ e^{-\sigma_{pk}(z_1-z)} + t_k^- e^{-\sigma_{pk}(z-z_2)}, \quad k = 1, 2 \\ \Psi_m(\alpha, z) &= \mathfrak{F}_{x,y}[\psi_m] = t_{2+m}^+ e^{-\sigma_s(z_1-z)} + t_{2+m}^- e^{-\sigma_s(z-z_2)}, \quad m = 1, 2. \end{aligned} \tag{21}$$

where

$$\alpha = \sqrt{\alpha_1^2 + \alpha_2^2}, \quad \sigma_{pk} = \sqrt{\alpha^2 - \varkappa_{pk}^2}, \quad (k = 1, 2), \quad \sigma_s = \sqrt{\alpha^2 - \varkappa_s^2}.$$

The branches of the square roots for σ were chosen so that

$$\text{Re } \sigma \geq 0, \quad \text{Im } \sigma \leq 0$$

for real α in accordance with the limiting absorption principle [60]. Meanwhile, the relations (21) are expressed via exponentially decaying terms ($z_2 \leq z \leq z_1 \leq 0$), which provide numerical stability.

Due to the isotropic property of the materials considered in this investigation, axisymmetric terms can be extracted from the displacement and stress fields. Therefore, applying the Fourier transform and the linear transformation:

$$\mathbf{B} = \begin{pmatrix} 0 & 0 & 1 \\ i\alpha_1/\alpha^2 & i\alpha_2/\alpha^2 & 0 \\ i\alpha_2/\alpha^2 & -i\alpha_1/\alpha^2 & 0 \end{pmatrix},$$

The Fourier transforms $\tilde{\mathbf{U}}_s(\alpha, z) = B\mathfrak{F}_{x,y}[\mathbf{u}_s]$, $\tilde{\mathbf{U}}_f(\alpha, z) = B\mathfrak{F}_{x,y}[\mathbf{u}_f]$, $\tilde{\mathbf{T}}(\alpha, z) = B\mathfrak{F}_{x,y}[\boldsymbol{\tau}_3]$, and $P_f(\alpha, z) = \mathfrak{F}_{x,y}[p_f]$ are also axisymmetric with respect to the Fourier transform parameters (α_1, α_2) :

$$\begin{aligned} \tilde{\mathbf{U}}_\gamma &= \{\Phi'_\gamma + \alpha^2\Psi_{\gamma 1}, \Phi_\gamma + \Psi'_{\gamma 1}, \Psi_{\gamma 2}\}^T, \quad \gamma = s, f, \\ \tilde{\mathbf{T}} &= \{\zeta_1\Phi_1 + \zeta_2\Phi_2 + 2\mu\alpha^2\Psi'_1, 2\mu\Phi'_s + \mu(2\alpha^2 - \varkappa_3^2)\Psi_1, \mu\Psi'_2\}^T, \\ P_f &= \frac{1}{\phi}[(Q + R\eta_1)\varkappa_{p1}^2\Phi_1 + (Q\eta_2 + R)\varkappa_{p2}^2\Phi_2]. \end{aligned} \tag{22}$$

Here,

$$\begin{aligned} \Phi_\gamma &= \eta_{\gamma 1}\Phi_1 + \eta_{\gamma 2}\Phi_2, \\ \Psi_{sk} &= \Psi_k, \quad \Psi_{fk} = \eta_3\Psi_k \end{aligned}$$

are the linear combinations of the potentials, whereas

$$\begin{aligned} \zeta_k &= 2\mu\alpha^2\eta_{sk} - ((P + Q)\eta_{sk} + (R + Q)\eta_{fk})\varkappa_{pk}^2, \\ \eta_{s1} &= \eta_{f2} = 1, \quad \eta_{s2} = \eta_2, \quad \eta_{f1} = \eta_1. \end{aligned}$$

Satisfying the boundary conditions (7), the generalized state vector $\mathbf{V}(\alpha, z) = \{\tilde{\mathbf{U}}_s, W_3, \tilde{\mathbf{T}}, P_f\}$, where $W_3 = \phi(\tilde{\mathbf{U}}_{s1} - \tilde{\mathbf{U}}_{f1})$, must be continuous at the interfaces between two dissimilar poroelastic layers. Employing Equations (21) and (22), the generalized state vector is written in matrix form as follows:

$$\begin{aligned} \mathbf{V} &= \mathbf{C}^+(z)\mathbf{t}^+ + \mathbf{C}^-(z)\mathbf{t}^-; \\ \mathbf{C}^+ &= \mathbf{M}^+(\alpha)\mathbf{G}(\alpha, z_1 - z), \quad \mathbf{C}^- = \mathbf{M}^-(\alpha)\mathbf{G}(\alpha, z - z_2). \end{aligned} \tag{23}$$

Here, the amplitude coefficient vectors $\mathbf{t}^\pm = \{t_1^\pm, t_2^\pm, t_3^\pm, t_4^\pm\}$ obey appropriate boundary conditions at the interfaces,

$$\mathbf{G} = \exp(-\mathbf{diag}\{\sigma_{p1}, \sigma_{p2}, \sigma_s\}z)$$

is the diagonal exponential matrix,

$$\begin{aligned} \mathbf{M}^\pm &= \mathbf{M}(\alpha, \pm\sigma_{p1}, \pm\sigma_{p2}, \pm\sigma_s), \\ \mathbf{M}(\alpha, \sigma_1, \sigma_2, \sigma_3) &= \begin{pmatrix} \sigma_1 & \eta_2\sigma_2 & \alpha^2 \\ 1 & \eta_2 & \sigma_3 \\ d_{11} & d_{12} & d_{13} \\ d_{21} & d_{22} & d_{23} \\ d_{31} & d_{32} & d_{33} \\ d_{41} & d_{42} & d_{43} \end{pmatrix} \end{aligned}$$

and

$$\begin{aligned} d_{1k} &= \phi(\eta_{fk} - \eta_{sk})\sigma_k, \quad (k = 1, 2), \quad d_{13} = \phi(\eta_3 - 1)\alpha^2; \\ d_{2k} &= \zeta_k, \quad d_{23} = 2\mu\alpha^2\sigma_3; \\ d_{3k} &= 2\mu\eta_{sk}\sigma_k, \quad d_{33} = \mu(2\alpha^2 - \varkappa_s^2); \\ d_{4k} &= -(\eta_{sk}Q + \eta_{fk}R)\varkappa_k^2/\phi. \end{aligned}$$

For the case of a pure elastic isotropic layer, the solution is also of the form (23), where the generalized state vector $\mathbf{V} = \{\tilde{\mathbf{U}}_s, \tilde{\mathbf{T}}\}$ and matrices $\mathbf{M}(\alpha, \sigma_p, \sigma_s)$, and $\mathbf{G} = \exp(-\mathbf{diag}\{\sigma_p, \sigma_s\}z)$ is 6×2 -dimensional now. Here,

$$\sigma_p = \sqrt{\alpha^2 - \varkappa_p^2}, \quad \sigma_s = \sqrt{\alpha^2 - \varkappa_s^2}$$

and \varkappa_p, \varkappa_s are wavenumbers of P- and S-waves in the elastic medium.

3.2. ES-Matrix Method for a Layered and Functionally Graded Poroelastic Structure

The generalized state vector $\mathbf{V}(\alpha, z)$ can be found in the form of Equation (23) for a layered poroelastic structure \mathbb{S} as

$$\mathbf{V} = \mathbf{E}_{\mathbb{S}}^+ \mathbf{c}^+ + \mathbf{E}_{\mathbb{S}}^- \mathbf{c}^-, \tag{24}$$

where $\mathbf{E}_{\mathbb{S}}^{\pm}(\alpha, z)$ and their horizontal concatenation $\mathbf{E}_{\mathbb{S}} = [\mathbf{E}_{\mathbb{S}}^+, \mathbf{E}_{\mathbb{S}}^-]$ are stepwise matrix functions, the so-called matrices of the eigensolutions of the layered structure (ES-matrices), which were introduced in [51] for layered piezoelectric materials. The vector of the amplitude coefficients \mathbf{c}^+ has the same size as the vector \mathbf{t}^+ for the first layer of \mathbb{S} , while the vector \mathbf{c}^- is of the same size as the vector \mathbf{t}^- for the last layer of the structure in the representation (23) for the corresponding layers.

The ES-matrices' construction algorithm is recurrent. The ES-matrix \mathbf{E}_n of the layered structure $\mathbb{S}_n = \mathbb{S}_{n-1} \cup \mathbb{L}_n$ is obtained from the known ES-matrix \mathbf{E}_{n-1} of the laminate $\mathbb{S}_{n-1} = \bigcup_{j=1}^{n-1} \mathbb{L}_j$ and the ES-matrix $\mathbf{E}_{\mathbb{L}_n} = [\mathbf{C}_n^+, \mathbf{C}_n^-]$ of the layer \mathbb{L}_n as follows:

$$\mathbf{E}_n^{\pm} = \begin{cases} \mathbf{E}_{n-1}^{\pm} + \mathbf{E}_{n-1}^{\mp} \mathbf{T}^{\pm}, & z \in \mathbb{S}_{n-1}, \\ \mathbf{C}_n^{\pm} \mathbf{T}^{\pm}, & z \in \mathbb{L}_n \end{cases}, \quad \mathbf{E}_n^{\pm} = \begin{cases} \mathbf{E}_{n-1}^{\mp} \mathbf{R}^{\pm}, & z \in \mathbb{S}_{n-1}, \\ \mathbf{C}_n^{\pm} \mathbf{R}^{\pm} + \mathbf{C}_n^{\mp}, & z \in \mathbb{L}_n. \end{cases} \tag{25}$$

Here, the matrices \mathbf{C}_n^{\pm} are constructed like the matrices \mathbf{C}^{\pm} in Equation (23) just for appropriate material parameters of the layer \mathbb{L}_n . Constant matrices \mathbf{T}^{\pm} and \mathbf{R}^{\pm} should be determined from the boundary condition at the interface $x_3 = z_n$ between \mathbb{S}_{n-1} and \mathbb{L}_n :

$$\Lambda_{n-1,n} \mathbf{E}_n^{\pm}(z_n + \varepsilon) = \Lambda_{n,n-1} \mathbf{E}_n^{\pm}(z_n - \varepsilon) \text{ at } \varepsilon \rightarrow +0, \tag{26}$$

where matrices $\Lambda_{n-1,n}$ and $\Lambda_{n,n-1}$ are employed to determine the quantities for the boundary conditions (7) or (8). Therefore, if the contacting layers are of the same type, then these matrices are identity matrices, but if the contacting layers \mathbb{L}_{n-1} and \mathbb{L}_n are porous and pure elastic, respectively, then $\Lambda_{n-1,n} = \Lambda_{p,s}$ and $\Lambda_{n,n-1} = \Lambda_{s,p}$, where

$$\Lambda_{p,s} \mathbf{V} = \{\tilde{\mathbf{U}}_s, W_3, \tilde{\mathbf{T}}\}, \quad \Lambda_{s,p} \mathbf{V} = \{\tilde{\mathbf{U}}_s, 0, \tilde{\mathbf{T}}\}.$$

Satisfying the boundary condition (26), \mathbf{T}^{\pm} and \mathbf{R}^{\pm} in (25) can be obtained as blocks of the following matrix:

$$\begin{pmatrix} \mathbf{T}^+ & \mathbf{R}^+ \\ \mathbf{T}^- & \mathbf{R}^- \end{pmatrix} = \mathbf{W}^{-1} \mathbf{Z}, \tag{27}$$

where \mathbf{W} and \mathbf{Z} are expressed using horizontal concatenations of \mathbf{C}_n^{\pm} and \mathbf{E}_{n-1}^{\pm} as

$$\mathbf{W} = [\Lambda_{n-1,n} \mathbf{C}_n^+(z_n), -\Lambda_{n,n-1} \mathbf{E}_{n-1}^-(z_n)],$$

$$\mathbf{Z} = [\Lambda_{n-1,n} \mathbf{E}_{n-1}^+(z_n), -\Lambda_{n,n-1} \mathbf{C}_n^-(z_n)].$$

The functionally graded porous layer \mathbb{L}_{loam} is simulated as a layered structure \mathbb{L}_{loam}^a with M homogeneous sublayers:

$$\mathbb{L}_{loam} \approx \mathbb{L}_{loam}^a(M) = \bigcup_{k=1}^M \mathbb{L}(\mathbb{M}_{loam}(\bar{d}_k), d_{k-1}, d_k), \tag{28}$$

where $\mathbb{M}_{loam}(\bar{d}_k)$ is the set of poroelastic properties of the loam slice calculated according to Equations (3) and (4) for fixed water saturation $\zeta(\bar{d}_k)$, $\bar{d}_k = \frac{1}{2}(d_{k-1} + d_k)$ and $d_k = z_1 k/M$.

For the known ES-matrix $E_{\mathbb{HS}}(\alpha, z)$ of the considered half-space HS, the displacements $\mathbf{u}_s(\mathbf{x}, \omega)$ and $\mathbf{u}_f(\mathbf{x}, \omega)$ are expressed in terms of the inverse Hankel transform as

$$\mathbf{u}_{\gamma}(\mathbf{x}, \omega) = \frac{1}{2\pi} \int_{\Gamma} \mathbf{K}_{\gamma}(\alpha, -i\frac{\partial}{\partial x}, -i\frac{\partial}{\partial y}, z) \mathbf{Q}(\alpha) J_0(\alpha r) \alpha d\alpha, \quad \gamma \in \{s, f\}, \tag{29}$$

where $Q = \mathfrak{F}_{x,y}[q]$ and $K_\gamma(\alpha, \alpha_1, \alpha_2, z) = \mathfrak{F}_{x,y}[k_\gamma(x, y, z)]$ are the Fourier transforms of the surface load and Green’s matrix k_γ , respectively, while $J_0(z)$ is the Bessel function of the first kind of zero order. The infinite path Γ goes along the real axis and surrounds the real poles $\alpha = \zeta$ of matrix K_γ in accordance with the limiting absorption principle [41,61]. Green’s matrices have the following form:

$$K_\gamma = B^{-1} \tilde{K}_\gamma B = \begin{pmatrix} -i(\alpha_1^2 M_\gamma + \alpha_2^2 N_\gamma)/\alpha^2 & -i\alpha_1\alpha_2(M_\gamma - N_\gamma)/\alpha^2 & -i\alpha_1 P_\gamma \\ -i\alpha_1\alpha_2(M_\gamma - N_\gamma)/\alpha^2 & -i(\alpha_2^2 M_\gamma + \alpha_1^2 N_\gamma)/\alpha^2 & -i\alpha_2 P_\gamma \\ \alpha_1 S_\gamma/\alpha^2 & \alpha_2 S_\gamma/\alpha^2 & R_\gamma \end{pmatrix}, \quad (30)$$

where the matrix:

$$\tilde{K}_\gamma = \Lambda_{u\gamma} E_{\mathbb{H}\mathbb{S}}^+(\alpha, z) (\Lambda_{load} E_{\mathbb{H}\mathbb{S}}^+(\alpha, 0))^{-1} \quad (31)$$

can be simplified and rewritten as the matrix of the axisymmetric solutions for unitary axisymmetric loads as follows:

$$\tilde{K}_\gamma(\alpha, z) = \begin{pmatrix} R_\gamma & S_\gamma & 0 \\ P_\gamma & M_\gamma & 0 \\ 0 & 0 & N_\gamma \end{pmatrix}.$$

The linear operators Λ_{load} and $\Lambda_{u\gamma}$ applied to the wavefield V are defined as

$$\Lambda_{load} V = \{\tilde{T}, P_f\}, \quad \Lambda_{u\gamma} V = \tilde{U}_\gamma.$$

Matrix K_γ in integral representation (29) obtained after substituting the derivatives with respect to the spatial coordinates x and y for α_1 and α_2 , respectively, becomes a differential operator applied to $J_0(\alpha r)$ [61].

4. Results

Let us consider three-layered strata: the poroelastic loam layer of thickness $a_1 = 1$ m subjected to the process of water infiltration, the poroelastic fully water saturated sand layer of thickness $a_2 = 1$ m, and the pure elastic bedrock. The elastic parameters of the considered materials taken in [62] are shown in Table 1. The loam hydrological parameters are the following:

$$\theta_r = 0, \quad \theta_s = 0.463, \quad n = 1.56, \quad l = 0.5, \quad \alpha_h = 3.5 \text{ (1/m)}, \quad K_s = 0.2496 \text{ (m/day)}.$$

Table 1. Material poroelastic parameters.

Material	ρ_s kg/m ³	K_s GPa	μ MPa	ϕ	ρ_f kg/m ³	K_f MPa	K_d MPa	α_s	$\kappa_s \cdot 10^{13}$ m ²	$\eta_f 10^6$ N s/m ²
water-saturated loam	2650	35	6.3	0.463	997	$2.25 \cdot 10^3$	17.6	1.58	3.74	100
air-saturated loam	2650	35	6.3	0.463	1.1	0.145	17.6	1.58	3.74	18
water-saturated sand	2650	35	13.3	0.437	997	$2.25 \cdot 10^3$	35.3	1.64	3.74	100
bedrock	2600	52.7	15,600	0	–	–	–	–	–	–

4.1. Infiltration in Loam

The soil simulation domain was initialized with the water content θ varying linearly with depth. The water content at the top surface had an initial condition (IC) at just below the porosity value (0.463) and linearly reduced with depth to reach an IC value of 0.001 (just above the residual water content) at the bottom layer of the domain. This is an IC

scenario that well represents a dry soil domain being wetted from the top down and is encountered in reality during experiments to determine the hydraulic conductivity of the soil in the field using disk infiltrometers. Values just under θ_s and just above θ_r were used in order to not encounter computational errors in the numerical solution.

The finite element solution of Richards' equation for the representative volume of the loam ($1 \times 1 \times 1 \text{ m}^3$) provides the water saturation parameter $\zeta(t, x_3) = \bar{\theta}(t, x_3)/\phi$, where $\bar{\theta}(t, x_3)$ is the mean value of $\theta(t, x_1, x_2, x_3)$ over the plane coordinate (x_1, x_2) . The obtained saturation ζ is depicted in Figure 2 for times $t \in [0, 45]$ days. A significant deviation from the initial linear distribution of porous water content is observed. The water content decreases gradually in the upper part of the loam layer, while the water content increases in the second (bottom) part of the layer. Thus, the water saturation gradually levels off, reaching an almost constant value $\zeta = 0.47$ throughout the thickness of the layer at $t = 45$ days of the infiltration process. During infiltration, water partially and freely penetrates the layer of sand. It was further assumed that there is some runoff of water in the sand; therefore, the sand layer was assumed to be fully saturated.

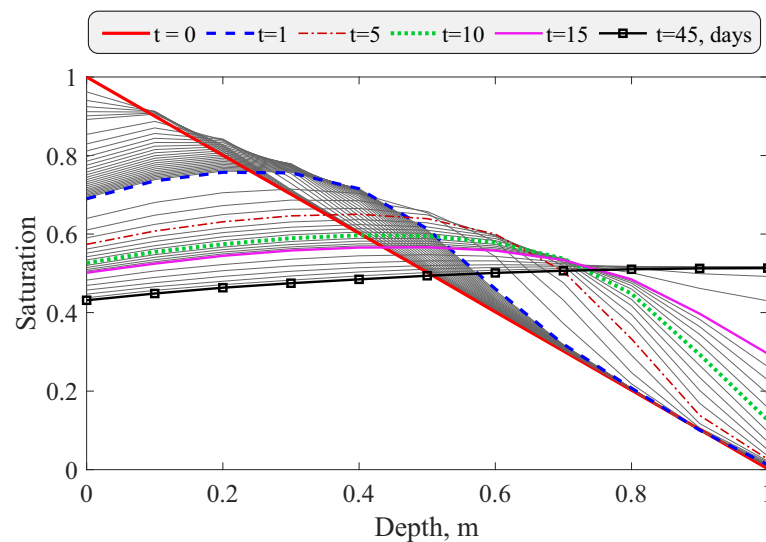


Figure 2. Water saturation $\zeta(z)$ changing per infiltration time t (in days) starting from the initial linear distribution.

4.2. Validation. Influence of Water Saturation on Surface Waves

To validate the developed method, let us consider the layered soil at $t = 1$ day of infiltration and excite the wave fields by a constant vertical load in a circle of radius $a = 1 \text{ m}$:

$$q(x) = \begin{cases} \{0, 0, 1\}, & r \leq a \\ \{0, 0, 0\}, & r > a \end{cases} .$$

The numerical satisfaction of displacements u_s, u_f by the governing Equations (1) and (5) in the layers of the structure is presented in Figure 3 for two frequencies: $f = 100 \text{ Hz}$ (Subplot a) and $f = 200 \text{ Hz}$ (Subplot b) at points $(1, 0, z)$ (m). The displacements are calculated using the numerical integration of the representation (29) with the relative error $\epsilon = 1 \times 10^{-5}$. Therefore, the derivatives for the governing Equations (1) and (5) are calculated numerically as well with the second-order-accurate formula with the relative error $\epsilon = 1 \times 10^{-5}$. Then, the obtained residuals for the governing equations are divided by the norm of the inertial part of the equations. The functionally graded loam is simulated as an M -layered medium described by the relations (28). To check the accuracy, the continuous properties $\mathbb{M}(z)$ are substituted into the governing Equations (1) and (2). Therefore, the relative error in the functionally graded loam is decaying with M , while it is stable in the homogeneous media (sand and bedrock).

The convergence of the developed method for functionally graded strata is demonstrated in Figure 4 by means of the vertical component of the Umov–Poynting vector e_z . For the case of a poroelastic medium, this component has the following representation [63]:

$$e_z = -\frac{\omega}{2} \text{Im}(\mathbf{u}_s \cdot \boldsymbol{\tau}_3 - w_3 p_f^*).$$

Here, p_f^* is the complex conjugation of the water pressure p_f . Due to continuity boundary conditions at the interfaces, the vertical component e_z is also continuous at interfaces z_k , which can be observed in Figure 4 for frequencies $f = 100$ and $f = 200$ Hz at points $(1, 0, z)$. Sufficient accuracy is already achieved at $M = 20$ for the considered frequency range (frequencies up to $f = 1000$ Hz).

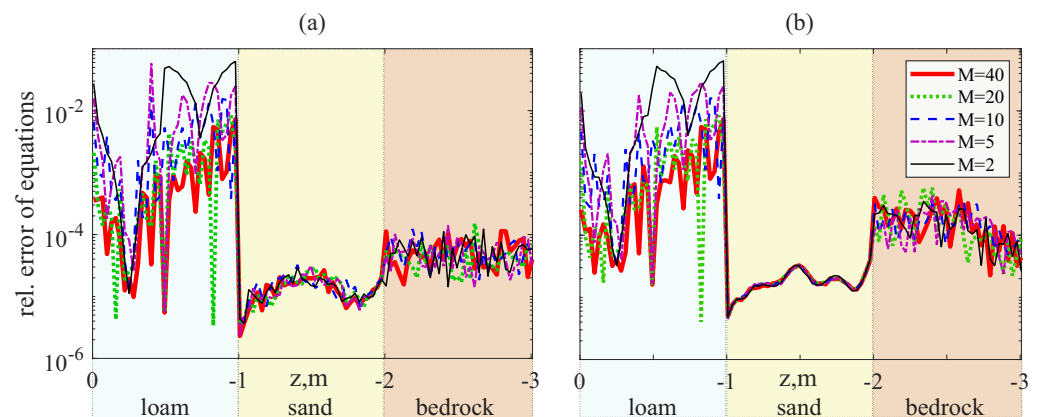


Figure 3. The relative residuals for the governing equations for the considered poroelastic strata at points (x, y, z) , where $x = 1$ m, $y = 0$, at frequencies $f = 100$ Hz (Subplot (a)) and $f = 200$ Hz (Subplot (b)) for different numbers of sublayers M simulating a loam layer affected by inhomogeneous infiltration at $t = 1$ day.

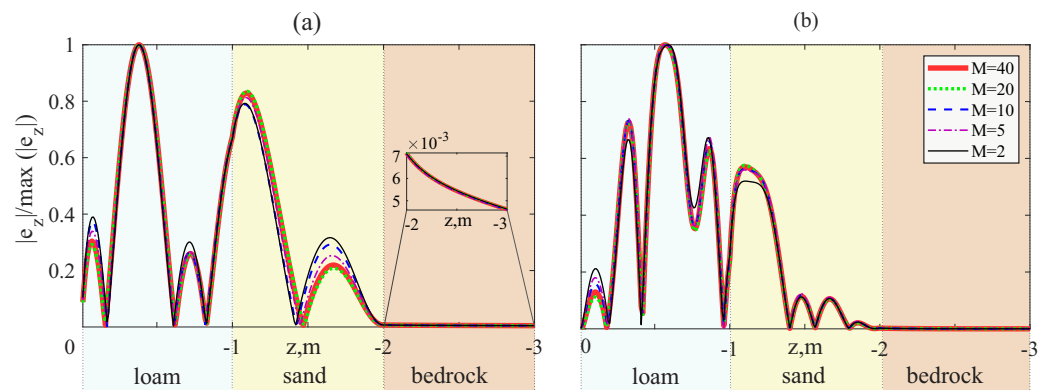


Figure 4. Vertical component $e_z(x, y, z)$ of Umov–Poynting vector for $x = 1$ m, $y = 0$ m at $f = 100$ Hz (a) and $f = 200$ Hz (b), $t = 1$ day of infiltration, and different numbers of loam sublayers M .

The slownesses s_n for the n -th guided wave are related to the wavenumber ζ_n as $s_n = \zeta_n/\omega$, where the magnitudes of ζ_n are the poles of the Fourier transform of Green’s matrix \mathbf{K}_γ . The rather fast convergence of the slownesses with the number of sublayers of loam M increase is observed. As an example, the dispersion curves, namely the real and imaginary parts of the slownesses–frequency relation $s_n(f)$, are shown in Figure 5 for the considered poroelastic three-layer strata. Here, the convergence with the variation of the number of sublayers M is also clearly demonstrated considering $M = 5, 10$, and 20 . All traveling waves determined here numerically have an attenuation due to pore fluid viscosity (see Figure 5b). The smallest attenuation ($\text{Im}s_n$) is

observed with the smallest slownesses ($Re s_n$). Here, we can also observe the relay transmission of guided waves due to the osculation or repulsion of modes, which was studied earlier for purely elastic laminates [64,65].

As the provided analysis has shown, the effect of infiltration on the guided waves' slowness can be observed. The most-significant effect is observed for the slowest guided wave ($n = 1$) at higher frequencies, as demonstrated in Figure 6. The real part of s_1 increases, while the attenuation ($Im s_1$) decreases with increasing infiltration time t . The most-significant changes in s_1 are observed during the first day of infiltration ($t \leq 1$).

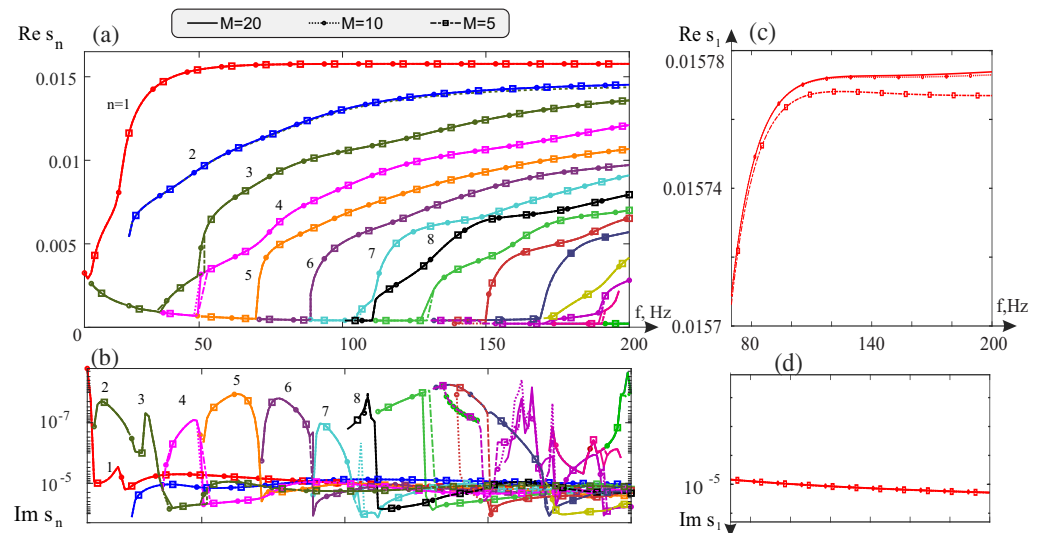


Figure 5. Convergence of dispersion curves: slowness $Re s_n$ (Subplot (a)) and attenuation $Im s_n$ (Subplot (b)) of guided waves excited at $t = 1$ day of infiltration as well as the zoom for $Re s_1$ (c) and $Im s_1$ (d).

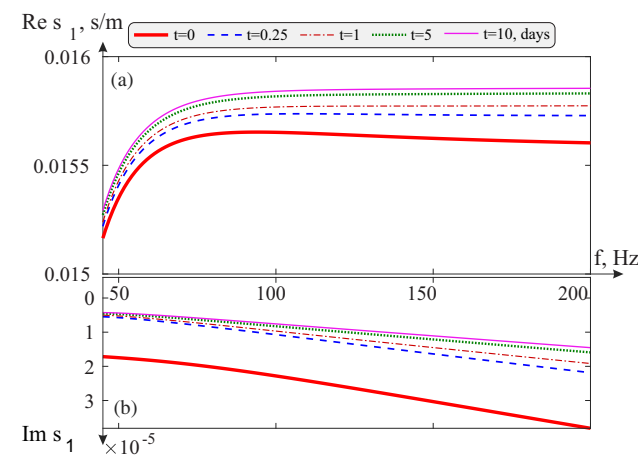


Figure 6. Slowness $Re s_1$ (Subplot (a)) and attenuation $Im s_1$ (Subplot (b)) of the first fundamental mode ($n = 1$) excited at different times t of porous water infiltration.

5. Discussion

The determination of the structure and water saturation of porous media is still a challenging task requiring extensive and time-consuming calculations since complex interactions in inhomogeneous and stratified media are to be accurately simulated. This study presented a two-stage poroelastic dynamic model for modeling wave propagation in partially saturated layered strata with the fluid saturation of the media depending on the infiltration time. The semi-analytical method based on the boundary integral equation method employed in the second stage of the simulations does not demand sufficient computational resources and provides accurate results quickly.

Sensors located at the surface of soil can register the characteristics of guided waves as the reciprocal of phase velocities [66]. Therefore, the proposed two-stage method can be further employed for the inverse problem solution, where the saturation can be determined, e.g., from the experimentally determined wavenumber–frequency relations for the propagating surface acoustic waves using the techniques for material properties' identification in an elastic waveguide [67–69]. The latter should rely on information about the dispersion characteristics of guided waves, which are extracted by applying the matrix pencil method, for instance.

The developed mathematical model is applicable to fast parametric analysis of surface acoustic wave propagation in various porous media due to its semi-analytical nature. It should also be noted that other relations for homogenization or explicit two-fluid model of poroelasticity [70,71] can be used to adjust the model to the experimental data.

Author Contributions: Conceptualization, S.I.F. and R.B.J.; methodology, S.I.F. and R.B.J.; software, S.I.F. and R.B.J.; validation, S.I.F. and R.B.J.; formal analysis, S.I.F., R.B.J. and M.V.G.; investigation, S.I.F., M.V.G. and R.B.J.; resources, S.I.F., M.V.G. and R.B.J.; data curation, S.I.F. and R.B.J.; writing—original draft preparation, S.I.F., M.V.G. and R.B.J.; writing—review and editing, S.I.F., M.V.G. and R.B.J.; visualization, S.I.F. and M.V.G.; project administration, S.I.F. All authors have read and agreed to the published version of the manuscript.

Funding: This research was funded by the Russian Science Foundation and the Kuban Science Foundation, Grant Number 22-21-20053.

Acknowledgments: The authors are grateful to E.V. Glushkov and N.V. Glushkova (Kuban State University, Krasnodar, Russia) for fruitful discussions on the presented methods and numerical results.

Conflicts of Interest: The authors declare no conflict of interest.

References

1. Glushkov, E.V.; Glushkova, N.V.; Evdokimov, A.A. Hybrid numerical-analytical scheme for calculating elastic wave diffraction in locally inhomogeneous waveguides. *Acoust. Phys.* **2018**, *64*, 1–9. [[CrossRef](#)]
2. Cheng, H.; Liu, Y.; Liang, D. Analyzing 3D Helmholtz equations by using the hybrid complex variable element-free Galerkin method. *Int. J. Comput. Mater. Sci. Eng.* **2023**, *12*, 2350005. [[CrossRef](#)]
3. Golub, M.; Fomenko, S.; Shpak, A.; Gu, Y.; Wang, Y.; Zhang, C. Semi-analytical hybrid approach for modeling guided wave-based SHM system for a laminate with multiple delaminations and surface-mounted inhomogeneities. *Appl. Math. Model.* **2023**, *120*, 812–832. [[CrossRef](#)]
4. Lo, W.C.; Sposito, G.; Majer, E. Wave propagation through elastic porous media containing two immiscible fluids. *Water Resour. Res.* **2005**, *41*, W02025. [[CrossRef](#)]
5. Ben Neria, A.; Assouline, S.; Shavit, U.; Weisbrod, N. Impact of ambient conditions on evaporation from porous media. *Water Resour. Res.* **2014**, *50*, 6696–6712. [[CrossRef](#)]
6. Teng, J.; Zhang, X.; Zhang, S.; Zhao, C.; Sheng, D. An analytical model for evaporation from unsaturated soil. *Comput. Geotech.* **2019**, *108*, 107–116. [[CrossRef](#)]
7. Henderson-Sellers, A. Soil moisture: A critical focus for global change studies. *Glob. Planet. Chang.* **1996**, *13*, 3–9. [[CrossRef](#)]
8. Vereecken, H.; Kasteel, R.; Vanderborght, J.; Harter, T. Upscaling hydraulic properties and soil water flow processes in heterogeneous soils: A review. *Vadose Zone J.* **2007**, *6*, 1–28. [[CrossRef](#)]
9. Van Genuchten, M.T. A closed-form equation for predicting the hydraulic conductivity of unsaturated soils. *Soil Sci. Soc. Am. J.* **1980**, *44*, 892–898. [[CrossRef](#)]
10. Spiridonov, D.; Vasilyeva, M.; Chung, E.T.; Efendiev, Y.; Jana, R. Multiscale model reduction of the unsaturated flow problem in heterogeneous porous media with rough surface topography. *Mathematics* **2020**, *8*, 904. [[CrossRef](#)]
11. Šimůnek, J.; Van Genuchten, M.T.; Šejna, M. The HYDRUS software package for simulating two- and three-dimensional movement of water, heat, and multiple solutes in variably-saturated porous media. *Tech. Man. Version* **2018**, *3*, 274.
12. Zhao, M.L. Finite Element Numerical Simulation of Two-Dimensional Unsaturated Soil Water Movement Problems. *Appl. Mech. Mater.* **2011**, *71*, 2933–2938. [[CrossRef](#)]
13. Scharnagl, B.; Vrugt, J.; Vereecken, H.; Herbst, M. Bayesian inverse modeling of in situ soil water dynamics: Using prior information about the soil hydraulic properties. *Hydrol. Earth Syst. Sci. Discuss.* **2011**, *8*, 2019–2063.

14. Vrugt, J.A.; Gupta, H.V.; Bouten, W.; Sorooshian, S. A Shuffled Complex Evolution Metropolis algorithm for optimization and uncertainty assessment of hydrologic model parameters. *Water Resour. Res.* **2003**, *39*, 1201 [CrossRef]
15. Yang, Y.; Mei, G. A Deep Learning-Based Approach for a Numerical Investigation of Soil–Water Vertical Infiltration with Physics-Informed Neural Networks. *Mathematics* **2022**, *10*, 2945. [CrossRef]
16. Jana, R.B.; Mohanty, B.P.; Springer, E.P. Multiscale Bayesian neural networks for soil water content estimation. *Water Resour. Res.* **2008**, *44*, W08408. [CrossRef]
17. Hu, W.; Liu, G.; Zhang, X. A pore-scale model for simulating water flow in unsaturated soil. *Microfluid. Nanofluid.* **2018**, *22*, 71. [CrossRef]
18. Novák, V.; Hlaváčiková, H.; Novák, V.; Hlaváčiková, H. Modelling of water flow and solute transport in soil. *Appl. Soil Hydrol.* **2019**, *32*, 319–337. [CrossRef]
19. Wang, T.; Stewart, C.E.; Ma, J.; Zheng, J.; Zhang, X. Applicability of five models to simulate water infiltration into soil with added biochar. *J. Arid. Land* **2017**, *9*, 701–711. [CrossRef]
20. Zou, C.; Zhang, S.; Jiang, X.; Chen, F. Monitoring and characterization of water infiltration in soil unsaturated zone through an integrated geophysical approach. *Catena* **2023**, *230*, 107243. [CrossRef]
21. Biot, M.A. Theory of propagation of elastic waves in a fluid-saturated porous solid. I. Low-frequency range. II. Higher frequency range. *J. Acoust. Soc. Am.* **1956**, *28*, 168–191. [CrossRef]
22. Frenkel, J. On the theory of seismic and seismoelectric phenomena in a moist soil. *J. Eng. Mech.* **2005**, *131*, 879–887. [CrossRef]
23. Pride, S.R.; Gangi, A.F.; Morgan, F.D. Deriving the equations of motion for porous isotropic media. *J. Acoust. Soc. Am.* **1992**, *92*, 3278–3290. [CrossRef]
24. Dell’Isola, F.; Igumnov, L.; Litvinchuk, S.Y.; Ipatov, A.; Petrov, A.; Modin, I. Surface waves in dissipative poroviscoelastic layered half space: Boundary element analyses. In *Dynamical Processes in Generalized Continua and Structures*; Springer: Berlin/Heidelberg, Germany, 2019; pp. 305–319.
25. Huang, L.; Liu, Z.; Wu, C.; Liang, J.; Pei, Q. A three-dimensional indirect boundary integral equation method for the scattering of seismic waves in a poroelastic layered half-space. *Eng. Anal. Bound. Elem.* **2022**, *135*, 167–181. [CrossRef]
26. Li, X.; Thomas, H.; Fan, Y. Finite element method and constitutive modeling and computation for unsaturated soils. *Comput. Methods Appl. Mech. Eng.* **1999**, *169*, 135–159. [CrossRef]
27. Zhao, C.; Li, W.; Wang, J. An explicit finite element method for Biot dynamic formulation in fluid-saturated porous media and its application to a rigid foundation. *J. Sound Vib.* **2005**, *282*, 1169–1181. [CrossRef]
28. Song, J.; Xu, C.; Feng, C.; Wang, F. An Explicit Finite Element Method for Saturated Soil Dynamic Problems and Its Application to Seismic Liquefaction Analysis. *Appl. Sci.* **2022**, *12*, 4586. [CrossRef]
29. Zhan, W.; Zhuang, M.; Liu, Q.Q.; Shi, L.; Sun, Y.; Liu, Q.H. Frequency domain spectral element method for modeling poroelastic waves in 3-D anisotropic, heterogeneous and attenuative porous media. *Geophys. J. Int.* **2021**, *227*, 1339–1353. [CrossRef]
30. Vershinin, A. Poroelastoplastic modeling of a borehole stability under small and finite strains using isoparametric spectral element method. In *Continuum Mechanics and Thermodynamics*; Springer: Berlin/Heidelberg, Germany, 2022; pp. 1–18.
31. Khoei, A.; Moallemi, S.; Haghghat, E. Thermo-hydro-mechanical modeling of impermeable discontinuity in saturated porous media with X-FEM technique. *Eng. Fract. Mech.* **2012**, *96*, 701–723. [CrossRef]
32. Wu, W.; Yang, Y.; Zheng, H. Hydro-mechanical simulation of the saturated and semi-saturated porous soil–rock mixtures using the numerical manifold method. *Comput. Methods Appl. Mech. Eng.* **2020**, *370*, 113238. [CrossRef]
33. Monforte, L.; Carbonell, J.M.; Arroyo, M.; Gens, A. Performance of mixed formulations for the particle finite element method in soil mechanics problems. *Comput. Part. Mech.* **2017**, *4*, 269–284. [CrossRef]
34. Jin, Y.F.; Yin, Z.Y. Two-phase PFEM with stable nodal integration for large deformation hydromechanical coupled geotechnical problems. *Comput. Methods Appl. Mech. Eng.* **2022**, *392*, 114660. [CrossRef]
35. Karim, M.; Nogami, T.; Wang, J. Analysis of transient response of saturated porous elastic soil under cyclic loading using element-free Galerkin method. *Int. J. Solids Struct.* **2002**, *39*, 6011–6033. [CrossRef]
36. Soares, D., Jr. Iterative dynamic analysis of linear and nonlinear fully saturated porous media considering edge-based smoothed meshfree techniques. *Comput. Methods Appl. Mech. Eng.* **2013**, *253*, 73–88. [CrossRef]
37. Deresiewicz, H.; Levy, A. The effect of boundaries on wave propagation in a liquid-filled porous solid: X. Transmission through a stratified medium. *Bull. Seismol. Soc. Am.* **1967**, *57*, 381–391. [CrossRef]
38. Parra, J.O.; Xu, P.C. Dispersion and attenuation of acoustic guided waves in layered fluid-filled porous media. *J. Acoust. Soc. Am.* **1994**, *95*, 91–98. [CrossRef]
39. Gorodetska, N. Wave Reflection from the free boundary of porous-elastic liquid-saturated half-space. *Int. J. Fluid Mech. Res.* **2005**, *32*, 327–339. [CrossRef]
40. Yan, S.G.; Xie, F.L.; Li, C.Z.; Zhang, B.X. Dispersion function of Rayleigh waves in porous layered half-space system. *Appl. Geophys.* **2016**, *13*, 333–342. [CrossRef]
41. Glushkov, E.; Glushkova, N.; Fomenko, S. Influence of porosity on characteristics of rayleigh-type waves in multilayered half-space. *Acoust. Phys.* **2011**, *57*, 230–240. [CrossRef]

42. Kolesnikov, V.; Suvorova, T.; Belyak, O. Modeling antifriction properties of composite based on dynamic contact problem for a heterogeneous foundation. *Mater. Phys. Mech.* **2020**, *46*, 139–148
43. Teymouri, H.; Khojasteh, A.; Rahimian, M.; Pak, R.Y. Wave motion in multi-layered transversely isotropic porous media by the method of potential functions. *Math. Mech. Solids* **2020**, *25*, 547–572. [[CrossRef](#)]
44. Shokrollahi, M.; Eskandari-Ghadi, M.; Khaji, N. A unified approach for stress wave propagation in transversely isotropic elastic and poroelastic layered media. *Soil Dyn. Earthq. Eng.* **2022**, *157*, 107152. [[CrossRef](#)]
45. Dudarev, V.V.; Mnukhin, R.M.; Vatulyan, A.O.; Nedin, R.D.; Gusakov, D.V. On the determination of the Biot modulus of poroelastic cylinder. *ZAMM J. Appl. Math. Mech. Z. Angew. Math. Mech.* **2019**, *99*, e201800137. [[CrossRef](#)]
46. Manna, S.; Anjali, T. Rayleigh type wave dispersion in an incompressible functionally graded orthotropic half-space loaded by a thin fluid-saturated aeolotropic porous layer. *Appl. Math. Model.* **2020**, *83*, 590–613. [[CrossRef](#)]
47. Manna, S.; Pramanik, D.; Althobaiti, S. Love-type surface wave propagation due to interior impulsive point source in a homogeneous-coated anisotropic poroelastic layer over a non-homogeneous extended substance. In *Waves in Random and Complex Media*; Taylor & Francis: Abingdon, UK, 2022; pp. 1–37.
48. Pradhan, N.; Saha, S.; Samal, S.K.; Pramanik, S. Nonlocal analysis of Rayleigh-type wave propagating in a gradient layered structure. *Eur. Phys. J. Plus* **2023**, *138*, 410. [[CrossRef](#)]
49. Glushkov, Y.V.; Glushkova, N.V.; Yeremin, A.A.; Mikhas'kiv, V.V. The layered element method in the dynamic theory of elasticity. *J. Appl. Math. Mech.* **2009**, *73*, 449–456. [[CrossRef](#)]
50. Ba, Z.; Zhang, E.; Liang, J.; Lu, Y.; Wu, M. Two-dimensional scattering of plane waves by irregularities in a multi-layered transversely isotropic saturated half-space. *Eng. Anal. Bound. Elem.* **2020**, *118*, 169–187. [[CrossRef](#)]
51. Fomenko, S.I.; Golub, M.V.; Doroshenko, O.V.; Wang, Y.; Zhang, C. An advanced boundary integral equation method for wave propagation analysis in a layered piezoelectric phononic crystal with a crack or an electrode. *J. Comput. Phys.* **2021**, *447*, 110669. [[CrossRef](#)]
52. Chen, Y.; Uchimura, T.; Irfan, M.; Huang, D.; Xie, J. Detection of water infiltration and deformation of unsaturated soils by elastic wave velocity. *Landslides* **2017**, *14*, 1715–1730. [[CrossRef](#)]
53. Chen, Y.; Irfan, M.; Uchimura, T. Estimation of elastic wave velocity through unsaturated soil slope as function of water content and shear deformation. *Soils Found.* **2019**, *59*, 2180–2194. [[CrossRef](#)]
54. Solazzi, S.G.; Bodet, L.; Holliger, K.; Jougnot, D. Surface-Wave Dispersion in Partially Saturated Soils: The Role of Capillary Forces. *J. Geophys. Res. Solid Earth* **2021**, *126*, e2021JB022074. [[CrossRef](#)]
55. Deng, T.; Hellwig, O.; Hlousek, F.; Kern, D.; Buske, S.; Nagel, T. Numerical modeling of seismic wave propagation in loosely deposited partially saturated sands: An application to a mine dump monitoring case. *Environ. Earth Sci.* **2023**, *82*, 200. [[CrossRef](#)]
56. Glushkov, E.V.; Glushkova, N.V.; Fomenko, S.I.; Zhang, C. Surface waves in materials with functionally gradient coatings. *Acoust. Phys.* **2012**, *58*, 339–353. [[CrossRef](#)]
57. Teja, A.; Rice, P. Generalized corresponding states method for the viscosities of liquid mixtures. *Ind. Eng. Chem. Fundam.* **1981**, *20*, 77–81. [[CrossRef](#)]
58. Sveshnikov, A.G. The limit absorption principle for a waveguide. *Dokl. Akad. Nauk USSR* **1951**, *80*, 345–347. (In Russian)
59. Šimůnek, J.; Van Genuchten, M.T.; Šejna, M. Recent developments and applications of the HYDRUS computer software packages. *Vadose Zone J.* **2016**, *15*. [[CrossRef](#)]
60. Babeshko, V.A.; Glushkov, E.V.; Zinchenko, J.F. *Dynamics of Inhomogeneous Linear-Elastic Media*; Nauka: Moscow, Russia, 1989. (In Russian)
61. Glushkov, E.V.; Glushkova, N.V. On the efficient implementation of the integral equation method in elastodynamics. *J. Comput. Acoust.* **2001**, *9*, 889–898. [[CrossRef](#)]
62. Lo, W.C.; Yeh, C.L.; Jan, C.D. Effect of soil texture and excitation frequency on the propagation and attenuation of acoustic waves at saturated conditions. *J. Hydrol.* **2008**, *357*, 270–281. [[CrossRef](#)]
63. Umov, N.A. *The Equations of Motion of the Energy in Bodies*; State Publishers of Technical-Theoretical Literature (GITTL): Moscow, Russia, 1950. (In Russian)
64. Glushkov, E.; Glushkova, N.; Fomenko, S. Wave energy transfer in elastic half-spaces with soft interlayers. *J. Acoust. Soc. Am.* **2015**, *137*, 1802–1812. [[CrossRef](#)]
65. Gravenkamp, H.; Plestenjak, B.; Kiefer, D.A. Notes on osculations and mode tracing in semi-analytical waveguide modeling. *Ultrasonics* **2023**, *135*, 107112. [[CrossRef](#)]
66. Irfan, M.; Uchimura, T. Development and Performance Evaluation of Disk-Type Piezoelectric Transducer for Measurement of Shear and Compression Wave Velocities in Soil. *J. Earthq. Eng.* **2018**, *22*, 147–171. [[CrossRef](#)]
67. Lu, L.; Charron, E.; Glushkov, E.; Glushkova, N.; Bonello, B.; Julien, F.H.; Gogneau, N.; Tchernycheva, M.; Boyko, O. Probing elastic properties of nanowire-based structures. *Appl. Phys. Lett.* **2018**, *113*, 161903. [[CrossRef](#)]
68. Golub, M.V.; Doroshenko, O.V.; Arsenov, M.; Bareiko, I.; Eremin, A.A. Identification of material properties of elastic plate using guided waves based on the matrix pencil method and laser Doppler vibrometry. *Symmetry* **2022**, *14*, 1077. [[CrossRef](#)]
69. Delory, A.; Lemoult, F.; Eddi, A.; Prada, C. Guided elastic waves in a highly-stretched soft plate. *Extrem. Mech. Lett.* **2023**, *61*, 102018. [[CrossRef](#)]

70. Lo, W.C.; Lee, J.W. Effect of water content and soil texture on consolidation in unsaturated soils. *Adv. Water Resour.* **2015**, *82*, 51–69. [[CrossRef](#)]
71. Barak, M.; Kumar, M.; Kumari, M.; Singh, A. Inhomogeneous wave propagation in partially saturated soils. *Wave Motion* **2020**, *93*, 102470. [[CrossRef](#)]

Disclaimer/Publisher’s Note: The statements, opinions and data contained in all publications are solely those of the individual author(s) and contributor(s) and not of MDPI and/or the editor(s). MDPI and/or the editor(s) disclaim responsibility for any injury to people or property resulting from any ideas, methods, instructions or products referred to in the content.